The Structural Colors of Photonic Glasses

Lukas Schertel[+,], Lukas Siedentop[*], Janne-Mieke Meijer, Peter Keim, Christof M. Aegerter, Geoffroy J. Aubry, Georg Maret[#]*

Keywords

isotropic structural colors, monodisperse colloidal glasses, disordered photonics, color modelling, gamut

Abstract

The color of materials usually originates from a combination of wavelength dependent absorption and scattering. Controlling the color without the use of absorbing dyes is of practical interest, not only because of undesired bleaching properties of dyes but also regarding minimization of environmental and health issues. Color control without dyes can be achieved by tuning the material's scattering properties in controlling size and spatial arrangement of scatterers. Here, we use calibrated photonic glasses (PGs) which are isotropic materials made by random aggregation of non-absorbing, monodisperse colloidal polystyrene spheres, to generate a wide spectral range of purely structural, angular independent colors. Experimental reflectance spectra for different sized spheres compare well with a recent theoretical model, which establishes the latter as a tool for color mapping in PGs. It allows to determine the range of visible colors accessible in PGs as function of size, packing fraction and refractive index of scatterers. It also predicts color saturation on top of the white reflectance as function of the sample's optical thickness. Blue, green, and red are obtained even with low index, while saturated green, cyan, yellow and magenta can be reached in higher index PGs over several orders of magnitude of sample thickness.

Color has a major influence on everyday life, from decision making[1] to general well-being.[2] In nature, colored materials also play an important role in the evolutionary development of certain animals and plants.[3–6] Most colors in artificial materials such as paints, cosmetics and coatings are based on dyes and pigments, i.e. wavelength dependent light absorbing materials. Similarly, biological colors are often based on light absorbing proteins called chromophores. However, nature sometimes uses an alternative approach to create most brilliant colors, e.g. in bird feathers or butterfly wings, using wavelength selective scattering.[7–11] Their colors arise from interference of light scattered from inhomogeneities in the refractive index of the material, spaced

[*] Contributed equally.
Dr. L. Schertel
Department of Chemistry, University of Cambridge, Cambridge, United Kingdom
[+]e-mail: ls849@cam.ac.uk

Dr. L. Schertel, L. Siedentop, Dr. J.-M. Meijer, Dr. P. Keim, Dr. G. J. Aubry Prof. G. Maret,
Fachbereich Physik, Universität Konstanz, 78457 Konstanz, Germany
[#]e-mail: georg.maret@uni-konstanz.de

Dr. L. Schertel, Prof. C. M. Aegerter
Physik-Institut, Universität Zürich, 8057 Zürich, Switzerland

Dr. G. J. Aubry
Département de Physique, Université de Fribourg, 1700 Fribourg, Switzerland

Dr. J.-M. Meijer
Institute of Physics, University of Amsterdam, Amsterdam, Netherlands

at scales comparable to optical wavelengths. These materials create vivid structural colors that, by their operational principle, cannot bleach. Structural colored materials are of interest for coloration in future devices and consumables as they can be achieved with biocompatible and environmental friendly materials.[12]

Structural colors can arise from ordered as well as disordered photonic structures. Periodically ordered photonic structures such as opals where iridescent colors arise from Bragg diffraction are well established.[13–17] Their colors are, however, strongly dependent on the angle of view because of the periodicity of interparticle distance giving rise to narrow diffraction maxima. For certain applications in coatings, paints, as well as cosmetics, this angular dependency can be undesirable. The disordered counterpart of photonic crystals are photonic glasses (PGs), which are random assemblies of monodisperse spherical particles.[18] The isotropic nature of their microscopic structure enables PGs to have angle independent structural colors, isotropic transport properties, reflectance, transmittance, and photonic (pseudo) band gaps. While these multiple scattering systems were first recognized as improved white paint materials,[19,20] controlled resonant scattering in the visible range[21] allows PGs to produce bright angle independent structural colors even in relatively low refractive index materials.[10,22]

Although the preparation of PGs is relatively well explored[20,23,24], a limited range of colors was produced so far by self-assembly of monodisperse spheres to PGs.[25–27] Note, that more advanced approaches such as core-shell particles and hydrogels produced by microfluidics and non-equilibrium colloidal assembly[28–31] broadened that range of colors but these modifications do come at the expense of scalability of the production process and cost. The lack of a quantitative description of the range of isotropic structural colors in photonic glasses has hindered the potential of these low cost structures for real life applications. Several explanations of structural colors have been proposed so far. For instance, Noh and coworkers have shown the importance of short range correlations in the structure for the color appearance and proposed a model based on single and double scattering.[32,33] Later Magkiriadou *et al.* used a quantitative scattering model to explain isotropic structural color in these materials and propose that color appearance is dominated by backscattering resonances of individual particles.[26] They claim that saturated red and yellow cannot be obtained in PGs due to their limited range of reachable hues caused by a blue single particle resonance. Nevertheless, so far the origin of angle independent structural colors is not fully understood and no corresponding model to show the exact range of accessible colors of PGs has been established.

Here we show that a recently developed quantitative scattering model[24,34] can fully capture the observed isotropic structural colors of PGs produced so far and even predicts a full, repeating color spectrum in PGs. The model takes into account resonant Mie scattering, short-range positional correlations, optical near-field coupling of randomly packed, spherical scatterers as well as the sample's internal reflection at the boundary. The model predicts the reflectance spectra and the expected sample color solely from the scatterer size, refractive index, filling fraction and sample thickness. We compare the reflectance spectra calculated by the model to spectral reflectance measurements of polystyrene (PS) PGs over the entire visible spectrum. By varying the colloidal scatterer size we can obtain blue, green, red and purple colors repeatably, as predicted by the model. In addition, changing the effective sample thickness enables us to tune between vivid colors and white broadband reflectance. The good agree-

ment between the model and experiment for PS PGs enables us to map the parameter space and to predict the range of color hues for different refractive index photonic materials. We show that in higher index PGs e.g. made of titania[24], even saturated yellow, magenta, blue, and green can be achieved over four decades of sample thicknesses. Clearly, this model provides a theoretical handle to make use of PGs for structural colors in industrial applications.

As the optical appearance of materials is given by its reflectance spectrum, we calculate the reflectance spectra from the transport mean free path $\ell^\star$ predicted by the scattering model. $\ell^\star$ is the length scale over which the memory of the direction of light propagation is lost in the regime of strong multiple light scattering.[24,34] In the situation of high turbidity present in the PGs, the light transport is diffusive on large length scales and $\ell^\star$ can be seen as the step length in a random walk of photons. $\ell^\star$ actually quantifies the inverse turbidity and the scattering strength $\lambda/\ell^\star$, λ being the incident vacuum wavelength. On a scale smaller than $\ell^\star$, a case sketched in Figure 1, a), the light scattering is described by resonant Mie scattering of individual spherical scatterers[35] represented by the form factor $F(\theta)$ (θ being the scattering angle) indicated in green. Positional correlations between the scatterers (taken as hard non-interpenetrating spheres) result in interparticle interferences which are accounted for by the Percus-Yevick structure factor $S(\theta)$,[36] sketched in blue. The angular dependent local scattering intensity is $I(\theta) = F(\theta) \cdot S(\theta)$ and $1/\ell^\star$ is obtained from angular integration of $I(\theta)$ weighted by $\rho \cdot (1 - \cos(\theta))$, ρ being the scatterers number density.[37] Note that in the evaluation of $I(\theta)$ the choice of an appropriate effective refractive index n_{eff} of the overall material is crucial. In contrast to earlier introduced models,[26,32,37] the proposed model uses the energy coherent potential approximation (ECPA) for the effective refractive index n_{eff}[38,39] which automatically accounts for near field optical coupling between scatterers. For a detailed description of the model, see references[24,34], SI and Figure SI.1 for the respective contributions of $F(\theta)$, $S(\theta)$, and n_{eff} to $\ell^\star$.

We determine the PG reflectance spectra $R(\lambda)$ from $\ell^\star(\lambda)$ via the transmittance for a slab shaped sample calculated from the solution of the diffusion equation[40,41]

$$T(\lambda) = \frac{\ell^\star(\lambda) + z_0(\lambda)}{L + 2z_0(\lambda)} \ , \tag{1}$$

with $z_0(\lambda)$ being the extrapolation length and L the sample thickness. $z_0(\lambda)$ incorporates boundary conditions and internal reflections at the surface of the sample and is calculated via[40]

$$z_0(\lambda) = \frac{2}{3}\ell^\star(\lambda)\left(\frac{1 + R_i}{1 - R_i}\right) \ , \tag{2}$$

where R_i is the internal reflectivity calculated via the use of Fresnel's law and the Garnett effective refractive index.[42] From the transmittance we finally obtain the reflectance spectrum $R(\lambda) = 1 - T(\lambda)$.

In equation (1) the sample thickness L is, besides the particle radius r, refractive index and filling fraction, an experimentally accessible parameter. However, the sample thickness is difficult to control on a macroscopic scale in experiments, especially in thin samples as required for isotropic structural colors. A practical means to circumvent a precise thickness control is adding a strong broadband absorber such as carbon black (CB).[10,12] CB lowers the absorption length L_{a} in the PG sample and thus acts as a cut off length for the photon path length distribution. Physically, this process eliminates the contributions of long photon paths that generate the white appearance in $R(\lambda)$.

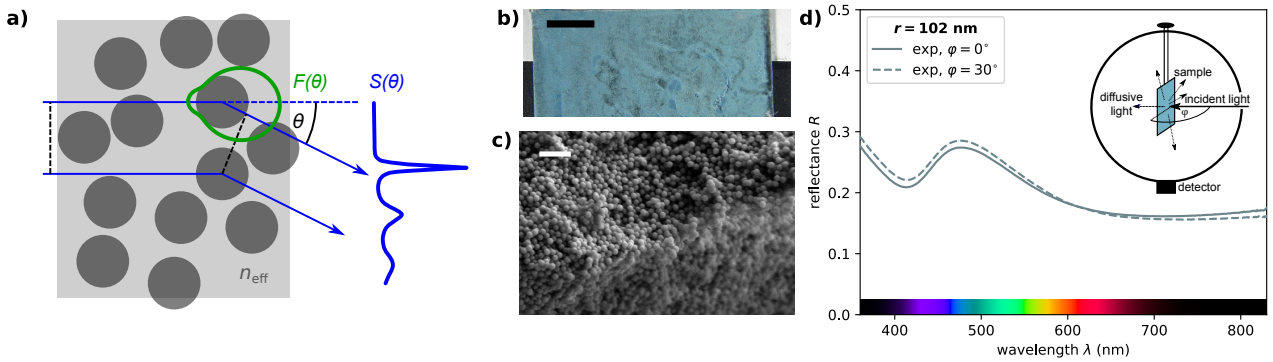

Figure 1: a) Sketch of the different contributions to the scattering in a PGs: Mie form factor $F(\theta)$ (green), hard sphere structure factor $S(\theta)$ (blue) and effective refractive index n_{eff} (grey) b): Photograph of a typical photonic glass consisting of monodisperse polystyrene spheres with radius $r = 93 \pm 2$ nm and 0.0125 wt% carbon black under diffusive white light illumination showing a blue color (scale bar: 0.5 cm). c): SEM micrograph of the sample in b) showing an edge (top and side view) of the random assembly (scale bar 1 μm). d): Measured reflectance spectra of the same sample under perpendicular illumination (angle of incidence $\varphi = 0°$) and under angled illumination ($\varphi = 30°$). Inset d): Sketch of the integrating sphere setup.

Controlling the amount of CB enables the preparation of macroscopically thick samples that still possess bright structural colors. The macroscopic absorption length L_{a} of such samples acts similar to an effective sample thickness L_{eff}. To be able to compare the calculated reflectance spectra of the model to experimental data, we replace L by L_{eff} in equation (1) and use it as a fitting parameter. Note that this is an approximation as the photon path length distribution is somewhat different for a non-absorbing sample of finite thickness L and a sample with a corresponding absorption length L_{a}. Note further that equation (1) is fully valid only in the diffusive limit $L \gg \ell^\star$, but may still be used here as a simple approximation for the calculation of R as the sample thickness L_{eff} is fitted in the model.

Having outlined the model calculation we now show a typical experimental PG. Figure 1, b) shows a photograph of a PG sample, where a blue structural color can be observed. We prepared the PG sample of PS spheres with $r = 93 \pm 2$ nm on a microscope slide according to the method of ref.[26] (For details see experimental section and Figure SI.2). A total concentration of 0.0125 wt% CB is present in the PG sample, which reduces the optical path length, as explained above. Figure 1, c) shows a typical SEM micrograph of the same sample, where the amorphous and random assembly of the spheres is visible. The reflectance spectra of the sample were measured as a function of wavelength using a UV-VIS spectrometer with an integrating sphere as detector unit under vertical illumination (angle of incidence $\varphi = 0°$) and angular illumination ($\varphi = 30°$). The normalized spectra for both angles of incidence are shown in Figure 1, d), where the inset shows a schematic of the integrating sphere setup. The clear similarity between both curves demonstrates the optical isotropy while the peak around 480 nm is responsible for the blue structural color.

In the following section we quantitatively compare our model to experimental spectra and explore the effect of scatterer size and sample thickness. A series of thirteen samples with particle sizes varying from $r = 59$ nm to $r = 251$ nm was prepared as described above. Figure 2, a) shows four representative PG samples consisting of PS spheres with $r = 147, 154, 174$ and 212 nm, respectively. A change of the particle radius r of less than 100 nm already leads to a dramatic change of the observed isotropic structural color hues. A crossover from purple to blue via green to dark red is observed in the photographs in Figure 2, a). The full series of particle sizes is shown in the SI in Fig-

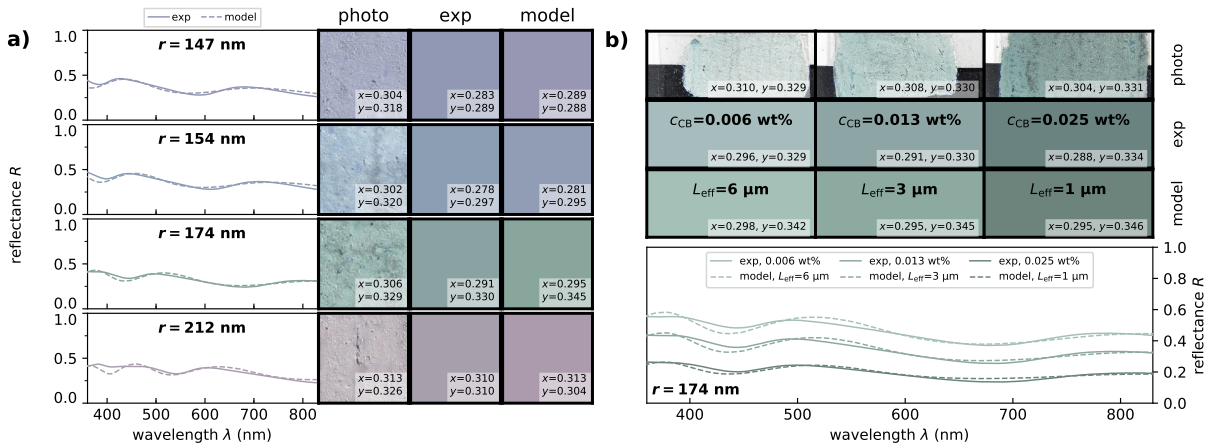

Figure 2: a) Radius sweep: Reflectance spectra of four PG samples with differing particle radius r, measured (exp, solid lines) and calculated (model, dashed lines). Photographs (area: 4x4 mm^2) of the measured samples (photo), color calculated from the measured spectrum (exp) and color calculated by the modeled spectrum (model). b) Effective thickness sweep (top to bottom): Photographs, measured colors, modeled colors, measured and modeled reflectance spectra for three different concentrations of CB (0.00625 wt%, 0.0125 wt%, 0.025 wt%). The corresponding effective sample thickness L_{eff} was fitted. White insets show the colors chromaticity coordinates.

ure SI.3 where even a repeating color sequence is observed. We measured reflectance spectra (solid lines) of each sample and compare them to the proposed model (dashed lines). In the model the experimentally determined radii are used without fitting, although a polydispersity of 5% is employed to account for the small experimental polydispersity. In addition, a filling fraction of $f = 0.3$ is used which is similar to the earlier experimentally verified value for dried PGs.[24] Note that this filling fraction is relatively low compared to the sediment value obtained directly after centrifugation, but slipcasting and drying leads to a network like packing rather than to a dense particle packing. The only fitting parameter is the sample thickness L_{eff} that is determined via a least-squares fit. Very good agreement of the position of the observed resonances between the model and experimental curves is found. For the smallest particle size (r =93 nm), only the tail of the first resonance is observed in the low wavelength region, resulting in the dark blue color. The blue line in in SI Figure SI.1 shows the relevance of structural correlations for the position of the resonances. The first resonance is affected by structural correlations but the higher resonances are essentially not. With increasing r the resonance shifts from blue (r =93 nm) to green (r =114 nm) to red (r =128 nm). A second resonance appears in the low wavelength region of the spectrum of the sample with r =147 nm and explains its purple appearance. The shift of both resonances with further increasing particle size leads to the repeating color scheme observed in Figure 2, a). Note that for samples with larger particle radii the pure color appearance smears out as multiple resonances are present in the visible range of the spectrum.

The appearance of a second resonance with increasing r also explains earlier observations of blue dominated structural color in PGs.[26] However, our results show that this resonance does not eliminate intermediate colors like green and red but is very sensitive to a small change in r.

Besides the photographs, Figure 2, a) also shows the experimental and calculated spectra $R(\lambda)$ converted into colors as perceived by the human eye. The color sensation is approximated via the open-source python module colorpy[43], which allows to convert any spectrum in the visible range (we use the range $\lambda = [360, 830]$ nm) into a color space such as Commission internationale de l'éclairage (CIE) xyY or RGB,

making the color printable or displayable on a screen. See Figure SI.4 and, e.g., reference[44] for the derivation of the colorspaces and the xy-chromaticity coordinates. By comparing the chromaticity coordinates between the measured and the modeled spectrum, we see a remarkably good agreement between the colors of the measured and modeled spectrum as well as with the colors observed in the photographs.

The second parameter we investigated is the effect of absorption as controlled by the amount of CB which is equivalent to changing the effective sample thickness L_{eff}.[10,12] We prepared three samples with well defined concentrations of CB (0.00625 wt%, 0.0125 wt%, 0.025 wt%). Photographs of these samples are shown in Figure 2, b). Decreasing the CB concentration increases the effective sample thickness L_{eff}, changes the color saturation and generally leads to a lighter color appearance. Again, the model's L_{eff} value was fitted in the same manner to the experimental data. With increasing effective sample thickness, multiple scattering contributions become more relevant and the appearance becomes more whitish as the resonance amplitudes become smaller in respect to the mean reflectance. A crossover from vivid colors to white broadband reflectance can be seen with increasing sample effective thickness. The hue can be quantified by the chromaticity coordinates which are given in each color patch. We note that the effective thickness does not alter the hue significantly.

We are now able to use the proposed model and color conversion method to map the full relevant parameter space of isotropic structural colors for a specific refractive index of the particles. In Figure 3, a) we plot a map of colors calculated for PS PGs ($n = 1.6$) by the model, scanning the sample thickness and the particle radius. A filling fraction of $f = 0.3$ and a polydispersity of 5% was used as in the experiments. The corresponding colors of all the experimentally prepared PGs are indicated in the map as blue dots (Figure 2) or black crosses (SI Figure SI.3).

The color change with increasing particle size observed in Figure 2 is clearly visible in the maps. Note that a pure blue is only possible for very small particle sizes $r < 95$ nm in the crossover from Rayleigh to Mie-scattering and additionally for $r \approx 150$ nm. Changing the sample thickness (note the logarithmic scale) changes mainly the color saturation. The most intense colors of PS PG appear for particle radii between 50 nm and 300 nm and a effective sample thicknesses from 0.5 μm to 30 μm.

A prominent ingredient in white paints and other strongly multiple scattering materials is titanium dioxide (TiO_2) because of its high refractive index combined with low absorption in the visible. Strong resonant behavior was observed and understood with the ECPA scattering model in PGs of TiO_2 colloids .[24] In Figure 3, b) we show a map of PGs of perfectly spherical and monodisperse particles of $n = 2.0$ (amorphous TiO_2) and a filling fraction of $f = 0.5$. The higher index leads to more saturated colors due to the enhanced resonant scattering in these materials. We observe that for particle sizes of 100 nm to 150 nm strongly saturated yellow, magenta, cyan and green can be achieved over several orders of magnitude of sample thickness. The predicted saturated yellow and magenta in the TiO_2 map are in contrast to ref.[26], where an absence of saturated red and yellow was claimed in PGs.

Further quantification is given by calculating the points in CIE xy space that are possible to reach with a PG. We call this the gamut of the PG. The gamuts for PS PGs and TiO_2 PGs are shown in Figure 3, c), respectively d). The gamut is made up out of loops (each corresponding to a sample effective thickness sweep) that contain the whitepoint W: these are the high and

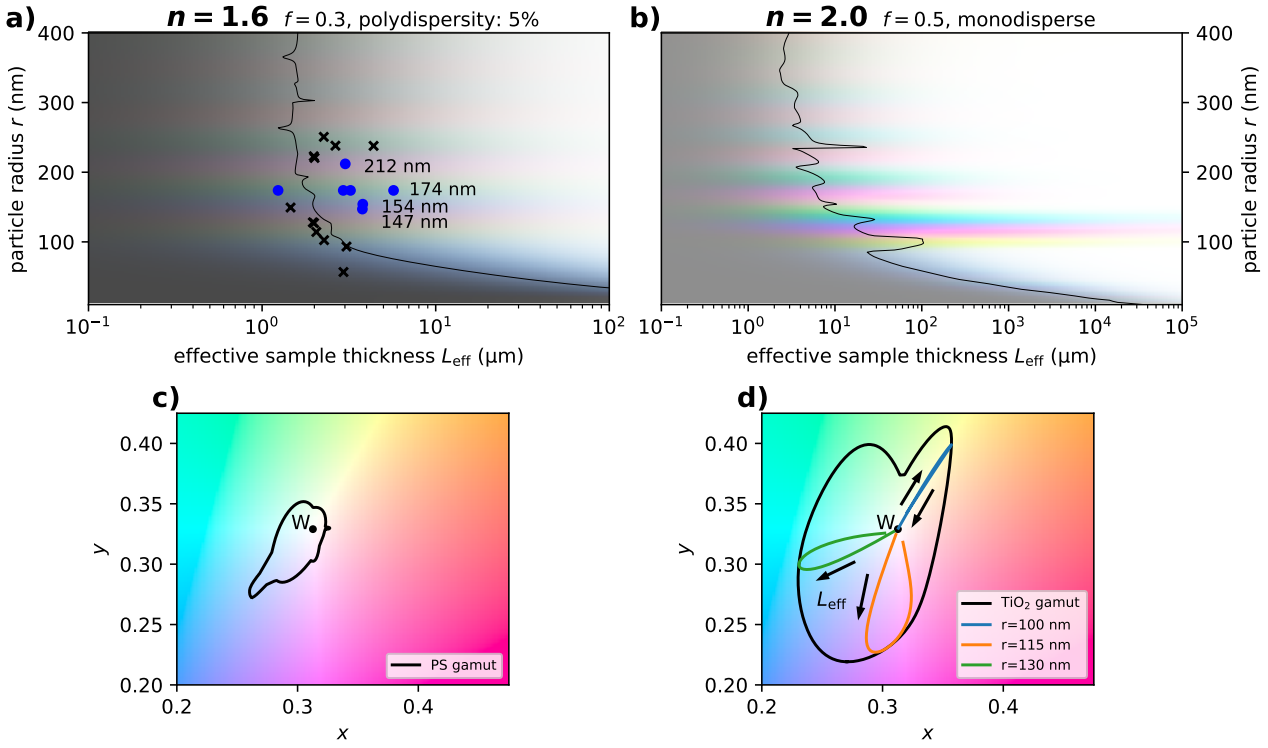

Figure 3: a) Color map for varying radius and sample thickness for a PG with refractive index $n = 1.6$, filling fraction $f = 0.3$ and a particle polydispersity of 5%. Blue dots correspond to the measured samples from Figure 2. Black crosses coresspond to samples of Figure SI.3. The black line indicates the sample thickness L that gives maximum color saturation for a corresponding particle radius r. b) Color map for a PG with refractive index $n = 2.0$, filling fraction $f = 0.5$ and no particle polydispersity. The black line indicates the maximum saturation as in a). c) and d) show the gamut reachable for PS PGs resp. TiO_2 PGs, i.e. the colors shown in a) resp. b). The three loops shown in d) correspond to a CB concentration sweep for three different radii. The arrows denote direction of increasing L_{eff}.

low limits of the effective sample thickness, where the sample is white and black respectively with vanishing color saturation. Three exemplary loops are shown in Figure 3, d). Changing the particle radius rotates the loop around the white point. There exists a sample thickness L for which the color is the most saturated for each r, i.e., the distance farthest away from the whitepoint. These L_{eff}-values of maximum saturation are shown in Figure 3 a) and b) as black lines. Note that our experimentally prepared PS samples are very close to these values. We observe that the point of maximum saturation for each loop does not make up the boundary of the gamut. This can especially be seen for $r = 115$ nm in d). To obtain the gamuts boundary, we calculate the CIE xy-values for a tightly sampled parameter space and calculated the convex hull via the k-nearest neighbour approach.[45] In terms of area of the complete visible gamut, we obtain 0.68 % for the PS PGs gamut and 4.28 % for the TiO_2 PGs gamut.

The asymmetry of the reachable area of colors around the white point in Figure 3 c) and d) shows the difficulty to obtain red and yellow. Note that for PS PGs, especially saturated blue is easily achievable (peak in the area to lower left corner). This might explain the increased occurrence of blue in natural structures such as bird feathers and beetles.[10,26]

In conclusion, we showed that even with low refractive index material (PS) blue, green, and red isotropic structural colors from photonic glasses can be prepared for a wide range of parameters. This might enable fabrication of biocompatible and sustainable paints and coatings by replacing current scatterer's materials with an environmental friendly material such as cellulose.[46,47] All our data are explained by a re-

cently proposed model.[24,34] The very good agreement of the predicted and observed isotropic structural colors allows us to use the model to predict the reachable color space for other refractive index materials. We show that saturated green, cyan, yellow and magenta can be reached in higher index PGs.[24] Other approaches such as coated spheres were used earlier to tune the contribution of structural correlations and Mie-scattering separately.[28] This allows to reach saturated colors in even lower index materials. Replacing the spherical bulk scatterers in the model by coated spheres would allow to predict colors even in these materials. Similarly, it was recognized that photonic structures found in nature often uses inverse structures[10], which is intrinsically included in the proposed scattering model.

Experimental section

Sample Preparation

Polystyrene spheres with different sizes ($r = 59$ nm to $r = 251$ nm) were obtained from microparticles GmbH. All PS spheres were characterized by TEM (Zeiss Libra120). For each particle, its size was determined for at least 100 particles. For more details see SI.

Photonic glasses were prepared according to the method of reference[26]. Typically, 800 μL of 5 wt% dispersion of monodisperse PS spheres in water was mixed with 50 μL aqueous dispersion containing 1 wt% carbon black (Cabot VXC72R) and 2 wt% Pluronic F-127 (Sigma-Aldrich). The Pluronic provides stabilization and keeps the CB particles suspended. Next, the mixture was centrifuged at 10000 rpm for 30 min and the supernatant was removed, thereby reaching a typical filling fraction of $f \approx 0.47 \pm 0.05$. The dense dispersion was slipcasted onto a microscope slide and the water was allowed to evaporate, resulting in an amorphous assembly of the spheres with a thickness of several hundred μm.

Sample Characterization

The structure of the particle assemblies were characterized in detail with SEM (Zeiss CrossBeam 1540XB). Samples were broken to reveal the inner structure of the PGs.

Color photographs of the PG samples on a white and black background were captured with a digital camera (Canon PowerShot SX30 IS, settings: 1/40 s exposure time, aperture F2.7, ISO 80, manual focus: 4.3 mm focal length) under illumination of white diffusive light from a halogen lamp (Intralux DC 1100 and Fiber-Lite PL-800). The images were normalized using the custom white balance of the camera to a white background (Figure 1, b)).

Reflectance spectra of the PG samples were measured in a UV-VIS spectrometer with an integrating sphere as detector unit (Agilent Cary 5000). Spectra were measured from 360 nm to 830 nm in 1 nm steps and with a spectral bandwidth (FWHM) of 2 nm. The circular illuminating beam had a diameter of ≈ 0.5 cm. A reference beam was used for calibration and a background (measurement without sample) was subtracted from the data. As the samples are relatively thick and contain CB, a strong broadband absorbing material, the remaining transmission can be assumed to be zero.

Acknowledgements

We thank Prof. Schmidt Mende for providing the Cary 5000 Spectrometer. We also acknowledge support by the Deutsche Forschungsgemeinschaft in the frame of SFB1214 project B2 and the Swiss National Science Foundation under project 200020M_162846. J.M. Mei-

jer acknowledges financial support from the Alexander von Humboldt Foundation.

Supporting Information

Supporting Information is available from the Wiley Online Library or from the author.

Conflict of Interest

The authors declare no conflict of interest.

[1] A. Bechara, H. Damasio, A. R. Damasio. *Cerebral Cortex* **2000**, *10*, 3 295.

[2] K. Yildirim, A. Akalin-Baskaya, M. Hidayetoglu. *Building and Environment* **2007**, *42*, 9 3233 .

[3] M. J. Ryan. *Science* **1998**, *281*, 5385 1999.

[4] S. M. Doucet, M. G. Meadows. *Journal of The Royal Society Interface* **2009**, *6*, suppl_2 S115.

[5] B. D. Wilts, K. Michielsen, H. De Raedt, D. G. Stavenga. *Proceedings of the National Academy of Sciences* **2014**, *111*, 12 4363.

[6] B. D. Wilts, X. Sheng, M. Holler, A. Diaz, M. Guizar-Sicairos, J. Raabe, R. Hoppe, S.-H. Liu, R. Langford, O. D. Onelli, D. Chen, S. Torquato, U. Steiner, C. G. Schroer, S. Vignolini, A. Sepe. *Advanced Materials* **2018**, *30*, 19 1702057.

[7] P. Vukusic, J. R. Sambles. *Nature* **2003**, *424* 852 EP .

[8] R. O. Prum, R. H. Torres, S. Williamson, J. Dyck. *Nature* **1998**, *396* 28 EP .

[9] P. Vukusic, J. R. Sambles, C. R. Lawrence, R. J. Wootton. *Proceedings of the Royal Society of London B: Biological Sciences* **1999**, *266*, 1427 1403.

[10] J. D. Forster, H. Noh, S. F. Liew, V. Saranathan, C. F. Schreck, L. Yang, J.-G. Park, R. O. Prum, S. G. J. Mochrie, C. S. O'Hern, H. Cao, E. R. Dufresne. *Advanced Materials* **2010**, *22*, 26-27 2939.

[11] E. S. A. Goerlitzer, R. N. Klupp Taylor, N. Vogel. *Advanced Materials* **2018**, *30*, 28 1706654.

[12] Y. Takeoka. *Chem. Commun.* **2018**, *54* 4905.

[13] E. Yablonovitch. *Phys. Rev. Lett.* **1987**, *58* 2059.

[14] E. Yablonovitch, T. J. Gmitter. *Phys. Rev. Lett.* **1989**, *63* 1950.

[15] C. López. *Advanced Materials* **2003**, *15*, 20 1679.

[16] G. von Freymann, V. Kitaev, B. V. Lotsch, G. A. Ozin. *Chem. Soc. Rev.* **2013**, *42* 2528.

[17] S. Kinoshita, S. Yoshioka, J. Miyazaki. *Reports on Progress in Physics* **2008**, *71*, 7 076401.

[18] J. Ballato. *J. Opt. Soc. Am. B* **2000**, *17*, 2 219.

[19] P. D. García, R. Sapienza, A. Blanco, C. López. *Advanced Materials* **2007**, *19*, 18 2597.

[20] P. D. García, R. Sapienza, C. López. *Advanced Materials* **2010**, *22*, 1 12.

[21] R. Sapienza, P. D. García, J. Bertolotti, M. D. Martín, A. Blanco, L. Viña, C. López, D. S. Wiersma. *Phys. Rev. Lett.* **2007**, *99*, 23 233902.

[22] B. Q. Dong, X. H. Liu, T. R. Zhan, L. P. Jiang, H. W. Yin, F. Liu, J. Zi. *Opt. Express* **2010**, *18*, 14 14430.

[23] M. Chen, D. Fischli, L. Schertel, G. J. Aubry, B. Häusele, S. Polarz, G. Maret, H. Cölfen. *Small* **2017**, *13*, 34 1701392.

[24] L. Schertel, I. Wimmer, P. Besirske, C. M. Aegerter, G. Maret, S. Polarz, G. J. Aubry. *Phys. Rev. Materials* **2019**, *3* 015203.

[25] Y. Takeoka, S. Yoshioka, A. Takano, S. Arai, K. Nueangnoraj, H. Nishihara, M. Teshima, Y. Ohtsuka, T. Seki. *Angewandte Chemie International Edition* **2013**, *52*, 28 7261.

[26] S. Magkiriadou, J.-G. Park, Y.-S. Kim, V. N. Manoharan. *Phys. Rev. E* **2014**, *90* 062302.

[27] H. Galinski, G. Favraud, H. Dong, J. S. T. Gongora, G. Favaro, M. Döbeli, R. Spolenak, A. Fratalocchi, F. Capasso. *Light: Science &Amp; Applications* **2017**, *6* e16233 EP , original Article.

[28] J.-G. Park, S.-H. Kim, S. Magkiriadou, T. M. Choi, Y.-S. Kim, V. N. Manoharan. *Angewandte Chemie International Edition* **2014**, *53*, 11 2899.

[29] J.-G. Park, W. B. Rogers, S. Magiriadou, T. Kodger, S.-H. Kim, Y.-S. Kim, V. N. Manoharan. *Optical Materials Express* **2017**, *7*, 1 253.

[30] L. Bai, V. C. Mai, Y. Lim, S. Hou, H. Möhwald, H. Duan. *Advanced Materials* **2018**, *30*, 9 1705667.

[31] G. Shang, L. Maiwald, H. Renner, D. Jalas, M. Dosta, S. Heinrich, A. Petrov, M. Eich. *Scientific Reports* **2018**, *8*, 1 7804.

[32] H. Noh, S. F. Liew, V. Saranathan, R. O. Prum, S. G. J. Mochrie, E. R. Dufresne, H. Cao. *Phys. Rev. E* **2010**, *81* 051923.

[33] H. Noh, S. F. Liew, V. Saranathan, S. G. J. Mochrie, R. O. Prum, E. R. Dufresne, H. Cao. *Advanced Materials* **2010**, *22*, 26-27 2871.

[34] G. J. Aubry, L. Schertel, M. Chen, H. Weyer, C. M. Aegerter, S. Polarz, H. Cölfen, G. Maret. *Phys. Rev. A* **2017**, *96*, 4 043871.

[35] C. F. Bohren, D. R. Huffman. *Absorption and Scattering of Light by Small Particles*. Wiley, New York, **1998**.

[36] J. K. Percus, G. J. Yevick. *Phys. Rev.* **1958**, *110* 1.

[37] S. Fraden, G. Maret. *Phys. Rev. Lett.* **1990**, *65* 512.

[38] K. Busch, C. M. Soukoulis. *Phys. Rev. Lett.* **1995**, *75* 3442.

[39] K. Busch, C. M. Soukoulis. *Phys. Rev. B* **1996**, *54* 893.

[40] N. Garcia, A. Z. Genack, A. A. Lisyansky. *Phys. Rev. B* **1992**, *46* 14475.

[41] M. Reufer, L. F. Rojas-Ochoa, S. Eiden, J. J. Sáenz, F. Scheffold. *Applied Physics Letters* **2007**, *91*, 17 171904.

[42] J. X. Zhu, D. J. Pine, D. A. Weitz. *Phys. Rev. A* **1991**, *44* 3948.

[43] M. Kness. Colorpy-a python package for handling physical descriptions of color and light spectra. `https://github.com/markkness/ColorPy`, **2008**. Accessed: 2019-01-18.

[44] D. Brainard, A. Stockman. In M. Brass, J. Enoch, E. Van Stryland, W. Wolfe, editors, *Handbook of optics (Volume III): vision and vision optics*, chapter 10. McGraw-Hill Education, **2010**.

[45] A. Moreira, M. Yasmina Santos. In *Proceedings of the Second International Conference on Computer Graphics Theory and Applications - Volume 1: GRAPP,*. INSTICC, SciTePress. ISBN 978-972-8865-71-9, **2007** 61–68.

[46] J. Zhang, T. J. Elder, Y. Pu, A. J. Ragauskas. *Carbohydrate Polymers* **2007**, *69*, 3 607 .

[47] C.-F. Yan, H.-Y. Yu, J.-M. Yao. *Cellulose* **2015**, *22*, 6 3773.

Supporting Information

Scattering Model

Figure SI.1 shows the scattering strength $\lambda/\ell^\star$ calculated by the scattering model introduced in detail in references[1,2] for a particle refractive index $n = 1.6$ and a filling fraction of $f = 0.3$ (black line) plotted versus the size ratio r/λ , with λ the incident wavelength and r the particle radius. The factors $S(\theta)$, $F(\theta)$ or n_{eff} used in the angular integral to calculate $\lambda/\ell^\star$ are respectively set to unity, while keeping the values for the two others (blue, green and grey dashed lines respectively) to show their relevance in the model. We observe that short-range structural correlations accounted for by $S(\theta)$ mainly influence the height and position of the first resonance (green vs. black curve), while Mie scattering in an effective medium represented by the form factor $F(\theta)$ is related to all resonances (blue vs. black). n_{eff} influences both, the height as well as the position of each resonance (dashed grey vs. black). Here the energy coherent potential approximation (ECPA) is used for the calculation of the effective refractive index[1,3] Changing this to the often used Garnett effective index n_{MG} smears out strongly resonant behavior (dotted dashed grey curve).

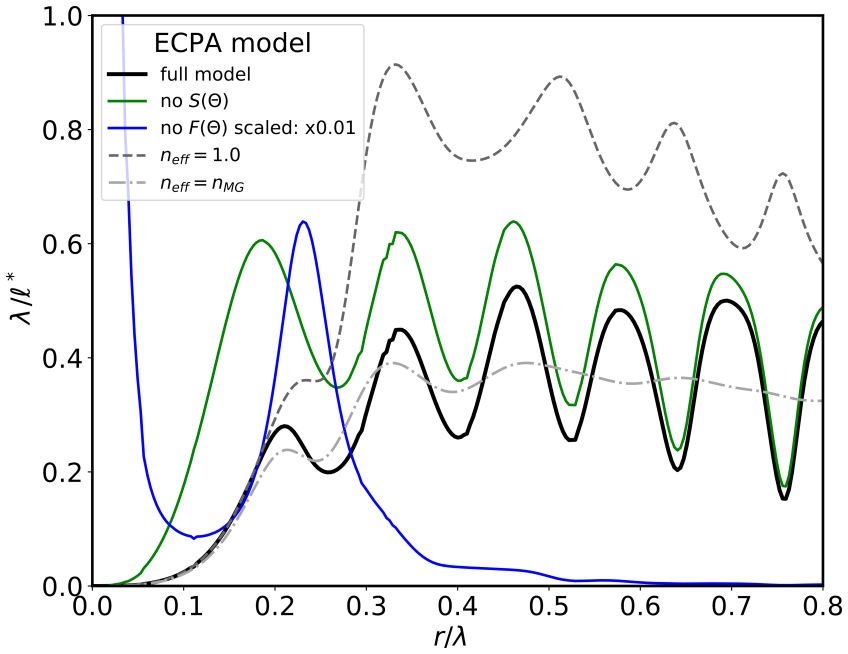

Figure SI.1: Scattering strength $\lambda/\ell^\star$ plotted versus size ratio r/λ for the ECPA scattering model[1,2] for $n = 1.6$ and $f = 0.3$ (black line). The same calculation performed with no structural correlation ($S(\theta) = 1$, green line), no single sphere resonance ($F(\theta) = 1$, blue line, scaled by 0.01) and without an effective index influence ($n_{\text{eff}} = 1$, grey dashed line) as well as using the Maxwell-Garnett value for the effective index ($n_{\text{eff}} = n_{\text{MG}}$, grey dashed dotted line).

Particle Characterization

All PS particles were characterized with TEM to verify their exact size, as the exact particle size is one of the most important parameters determining the structural color of PGs. The size was determined from the TEM micrographs via automated particle detection algorithms in ImageJ to provide the most accurate measurements. Figure SI.2, a) shows a typical TEM micrograph of PS spheres, with in the inset the measured size distribution.

Drying effect on PG surface

After slipcasting and drying the concentrated dispersions, a crystalline layer formed on the surface of the sample (see Figure SI.2, b)) due to strong capillary forces between the colloidal spheres. This top layer is undesired for quantitative comparison to the scattering model and was removed after drying by pressing lightly a sheet of paper on top and removing it after. Interestingly, it was found that this top layer enhances the isotropic structural color peaks in the reflectance spectra, as clearly seen in Figure SI.2, c).

Effect of scatterer size on structural color resonances

A series of thirteen samples with varying particle sizes from $r = 57$ nm to $r = 251$ nm was prepared. Figure SI.3 shows a full overview of all experimental and model reflectance spectra as well as photographs and the conversion of the spectra into observable colors.

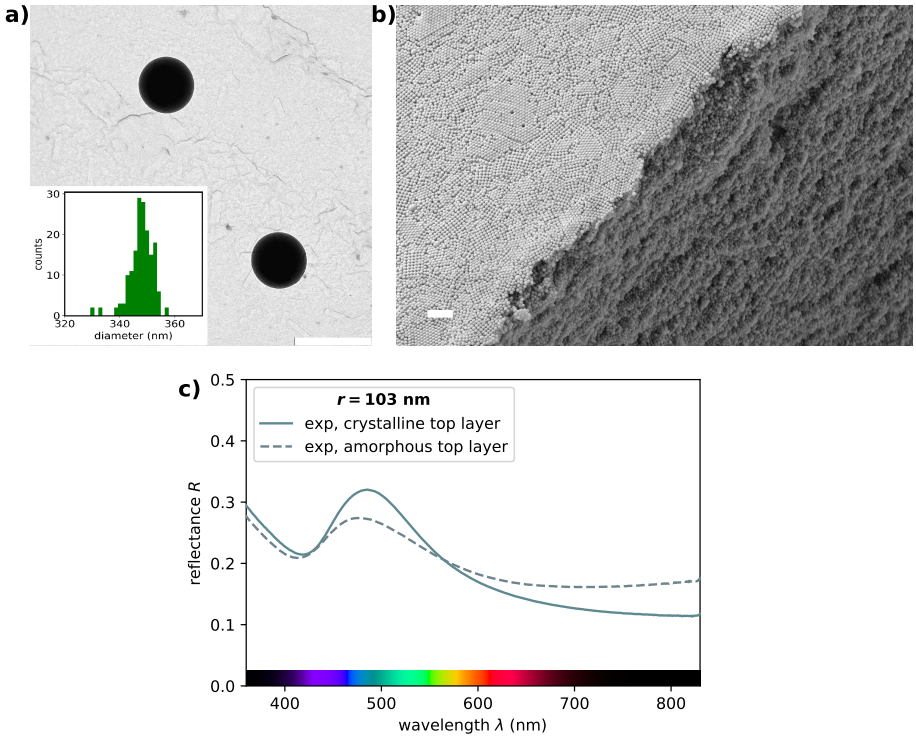

Figure SI.2: a) Typical TEM micrograph of PS spheres with $r = 174 \pm 3$ nm. (Scale bar 500 nm), Inset: Size distribution of the particles as determined with ImageJ. b) SEM micrograph of a sample with particles of radius $r = 250$ nm (scale bar 2 μm). c) Reflectance spectra of a PGs with particle size $r = 103$ nm with (solid line) and without (dashed line) crystalline monolayer on top.

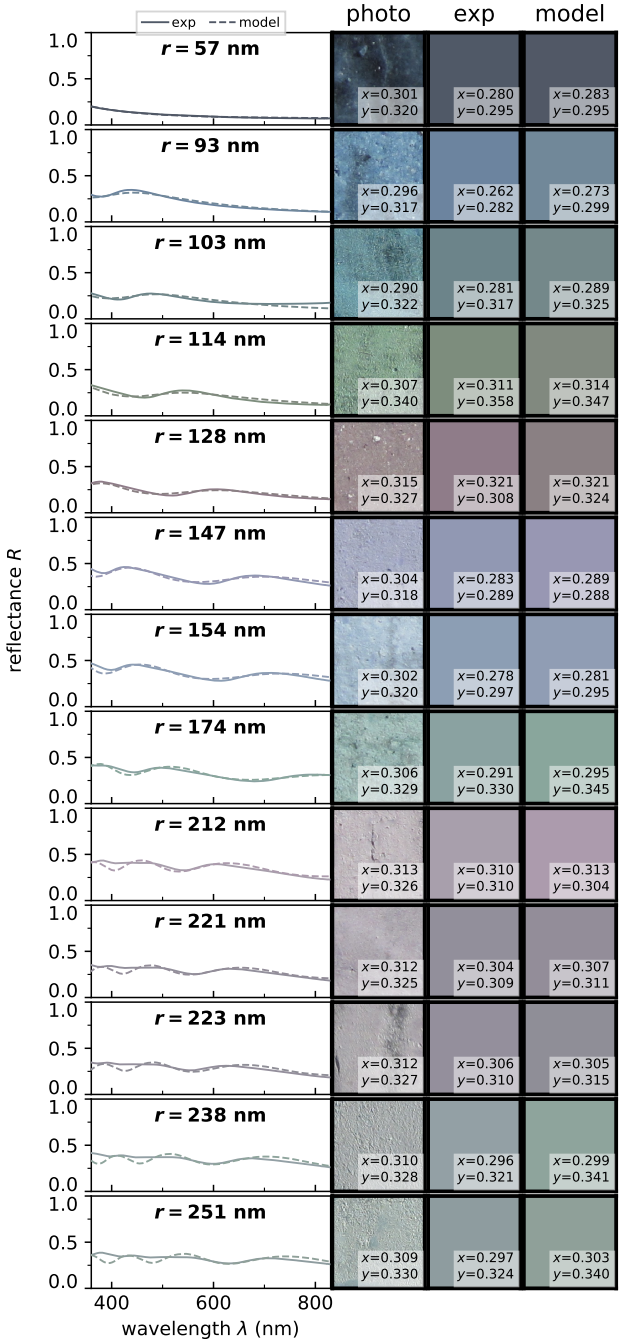

Figure SI.3: Same measurement as in Figure 2(a) for thirteen particle radii.

Spectrum to color conversion

Reflectance $R(\lambda)$ is the ratio of reflected to incident light intensity. Because the percepted color depends on the illumination, the reflectance-to-color conversion accounts for this by multiplying $R(\lambda)$ with a standard white illumination spectrum (Commission internationale de l'éclairage (CIE) Standard Illuminant D_{65}). This spectrum is then converted via the three CIE 1931 2° Standard Observers color matching functions to get the tristimulus in CIE XYZ colorspace. The tristimulus is converted to the normalized CIE xyY colorspace where $x = X/(X+Y+Z)$ and $y = Y/(X+Y+Z)$ are the chromaticity coordinates defining the colors hue and Y is the colors luminance. By normalizing to a certain luminance $Y = 1$, the whole range of colors —called *visible gamut*— can be located in a 2D plane spanned by x and y, see Figure SI.4. Its boundary is determined by the values for single wavelength colors in the visible range, where the endpoints at $\lambda = 360$ nm and $\lambda = 830$ nm are connected by the "line of purples". Any point in this convex area, including the D_{65} whitepoint, can be reached by a linear combination of at least two single line spectra. Color saturation is defined as the distance to this white point.

To print or represent the measured or modeled spectrum as a color on a display, a given xyY-point is further transformed to a linear RGB colorspace. This needs the definition of three primaries (red, green and blue) spanning the space: we use the ITU-R BT.709 standard phosphor chromaticities.[4] Note that these might differ from one displaying device to another, giving rise to potential color distortion. The RGB space is a subspace of the CIE xyY color space because the R, G and B points can only span a space inside of the visible gamut. Colors outside of this space will not be displayed correctly as the saturation stays constant with further distance to the whitepoint. The visible gamut and a color approximation of each xy-point is displayed in Figure SI.4, along with the single line spectra colors, the R, G and B primaries as well as a projection of the RGB space they are spanning.

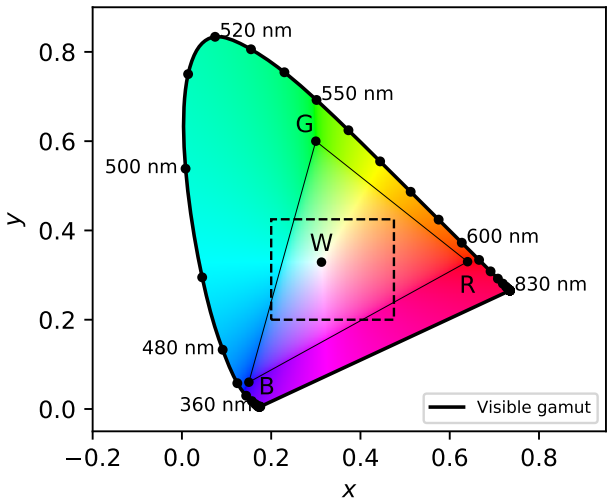

Figure SI.4: CIE xy chromaticity diagram with the RGB primaries and the subspace they are spanning. W denotes the D_{65} whitepoint. The visible gamut boundary arises from the single wavelength colors (annotated black line). The dashed rectangle shows the region of interest zoomed in in Figure 3, c) and d).

[1] G. J. Aubry, L. Schertel, M. Chen, H. Weyer, C. M. Aegerter, S. Polarz, H. Cölfen, G. Maret. *Phys. Rev. A* **2017**, *96*, 4 043871.
[2] L. Schertel, I. Wimmer, P. Besirske, C. M. Aegerter, G. Maret, S. Polarz, G. J. Aubry. *Phys. Rev. Materials* **2019**, *3* 015203.
[3] K. Busch, C. M. Soukoulis. *Phys. Rev. B* **1996**, *54* 893.
[4] Parameter values for the HDTV standards for production and international programme exchange . Standard, International Telecommunication Union, Geneva, CH, **2015**.